*remote sensing*

MDPI

*Article*

# Improved Phase Gradient Autofocus Method for Multi-Baseline Circular Synthetic Aperture Radar Three-Dimensional Imaging

**Shiliang Yi [1], Hongtu Xie [1,*], Yuanjie Zhang [1], Zhitao Wu [1], Mengfan Ge [1], Nannan Zhu [2], Zheng Lu [3] and Pengcheng Qin [4]**

[1] School of Electronics and Communication Engineering, Shenzhen Campus of Sun Yat-sen University, Shenzhen 518107, China; yishliang@mail2.sysu.edu.cn (S.Y.)
[2] School of Systems Science and Engineering, Sun Yat-Sen University, Guangzhou 510275, China
[3] Institute of Remote Sensing Satellite, China Academy of Space Technology, Beijing 100094, China
[4] Department of Weapons Engineering, Army Academy of Artillery and Air Defense, Hefei 230031, China
* Correspondence: xiehongtu@mail.sysu.edu.cn

**Abstract:** Multi-baseline circular synthetic aperture radar (MB CSAR) can be applied to obtain a three-dimensional (3D) image of the observation scene. However, the phase error caused by radar platform motion or atmospheric propagation delay restricts its 3D imaging capabilities. The phase error calibration of MB CSAR data is an essential step in the 3D imaging procedure due to the limited accuracy of positioning sensors. Phase gradient autofocus (PGA) is widely utilized to estimate the phase errors but is subject to shifts in the direction perpendicular to the line of sight and long iteration time in some sub-apertures. In this paper, an improved PGA method for MB CSAR 3D imaging is proposed, which can suppress the shifts and reduce computation time. This method is based on phase gradient estimation, but the prominent units are selected with an energy criterion. Then, weighted phase gradient estimation is presented to suppress the influence of prominent units with poor quality. Finally, a contrast criterion is adopted to reach faster convergence. The experimental results based on the measured MB CSAR data (Gotcha dataset) demonstrate the validity and feasibility of the proposed phase error calibration method for MB CSAR 3D imaging.

**Keywords:** multi-baseline circular synthetic aperture radar (MB CSAR); phase error calibration; three-dimensional (3D) imaging; weighted phase gradient autofocus (WPGA)

check for updates

**Citation:** Yi, S.; Xie, H.; Zhang, Y.; Wu, Z.; Ge, M.; Zhu, N.; Lu, Z.; Qin, P. Improved Phase Gradient Autofocus Method for Multi-Baseline Circular Synthetic Aperture Radar Three-Dimensional Imaging. *Remote Sens.* **2024**, *16*, 4242. https://doi.org/10.3390/rs16224242

Academic Editor: Stefano Perna

Received: 5 October 2024
Revised: 5 November 2024
Accepted: 12 November 2024
Published: 14 November 2024

**Copyright:** © 2024 by the authors. Licensee MDPI, Basel, Switzerland. This article is an open access article distributed under the terms and conditions of the Creative Commons Attribution (CC BY) license (https://creativecommons.org/licenses/by/4.0/).

## 1. Introduction

Synthetic aperture radar (SAR) technology is one of many radar technologies [1–3] and has great capabilities in imaging, target detection and terrain information extraction [4–7]. Thus, SAR has been widely applied in civilian and military fields, such as enemy reconnaissance, urban area imaging and farmland monitoring, showing huge potential for remote sensing application. Unlike optical sensors, SAR can achieve effective detection under poor-visibility conditions, like cloudy weather or nighttime [8], making it unique in its application scenarios. According to different requirements, SAR has derived various working modes, and multi-baseline circular SAR (MB CSAR) [9,10] is one of them. In this mode, airborne radar flies around the scene of interest with a 360-degree circular motion and flies along the same circular trajectory at different altitudes, forming multi-pass observations. MB CSAR can obtain the information of the scene from various directions and then form three-dimensional (3D) images.

In the field of MB CSAR 3D imaging technology, existing imaging methods are mainly divided into two categories, which are direct 3D imaging methods, such as 3D back-projection (3DBP) [11], and methods based on the principle of SAR tomography (TomoSAR) [12,13]. TomoSAR methods first perform two-dimensional (2D) imaging for each pass and then apply spectrum estimation methods such as Capon [14], multiple signal classification (MUSIC) [15] and compressed sensing (CS) [16] along the direction perpendicular

to the line of sight ($LOS_{\perp}$) for each pixel stack to achieve 3D images. A pixel stack refers to a set of complex pixel values located at the same position of 2D images but collected in different flying passes. TomoSAR methods are widely studied, since they are more time-efficient than directly projecting radar echo signals onto a 3D grid in the 3DBP method and also have the potential to achieve super-resolution in the $LOS_{\perp}$ direction. In ideal cases, the above imaging process can achieve good imaging results. However, in actual measurements, it is difficult for the radar platform to follow the ideal circular trajectory, and atmospheric propagation delay between trajectories often occurs. Such factors might cause phase errors along the $LOS_{\perp}$ direction. These phase errors can lead to a decrease in the main lobe, an increase in side lobes and even strong blur in the image. Furthermore, the accuracy of the positioning sensor is usually insufficient. Therefore, it is necessary to address phase error calibration before 3D imaging in the imaging process.

Scholars have conducted extensive research studies on the phase error calibration problem. The classical method refers data to a selected permanent scatterer (PS) or distributed (surface) scatterers (DSs) [17] and calibrates the phase error by measuring their phase information. However, this method assumes that the phase error is space-invariant or slowly changes in the scene of interest, so the calibration performance decreases when the points to be calibrated are far away from the PS. In 2006, Reigber et al. [18] estimated the phase error by modeling the baseline error from the interference result of two complex images. However, due to the assumption that the baseline error on the entire distance line is constant, phase errors may remain when the radar platform's motion state changes along the azimuth direction. In 2011, Gatti et al. [19] proposed algebraic altitude estimation (ALGAE), which can separate the surface reflection from other surface reflections. This method was verified on P-band SAR data obtained by the German Aerospace Center (DLR). However, this method requires full polarization multi-baseline SAR data and 2D phase unwrapping, resulting in a large computational burden. In 2016, the phase center double localization (PCDL) method was proposed [20]. This method can complete the calibration with only single-polarization data with lower computational complexity. However, its performance may be affected when the correlation between two images is low.

Autofocus is a kind of calibration method which can be mainly divided into two categories, criterion optimization and directly estimating the phase error. Criterion optimization autofocus methods allow the phase error within each pixel stack to be calibrated independently. In 2012, M. Pardini [21] used the minimum entropy criterion, with the entropy as the function to be optimized, and searched for the phase error that minimizes the entropy. However, in this method, shifts still exist in the $LOS_{\perp}$ direction. In [22], the cyclic coordinate descent approach was used to search for the phase error under the minimum entropy criterion. In [17], the phase derivative constrained optimization (PDCO) method was proposed, which provides and compares contrast and entropy as the optimization criteria. In the PDCO method, the second derivative of the phase error is searched instead of the phase error itself, solving the position shift problem by constraining the phase derivative. Sharpness optimization autofocus (SOA) [23,24] is an algorithm where estimation is based on coordinate descent but without the need to search. Since sharpness is defined by the square of the intensity, which is rather uncomplicated, an analytical solution is derived, saving the time cost caused by searching.

Autofocus methods of another kind estimate the phase error from the echo data or image data directly. Unlike the criterion-based methods, the phase error cannot be calculated pixel by pixel with such methods, since it is assumed that the phase error is space-invariant. Therefore, they are generally more suitable for smaller scenes. Phase gradient autofocus (PGA) was first applied in 2D imaging in [25,26]. This algorithm does not require a metric for optimization, but directly estimates the phase gradient from the echo data and can theoretically estimate phase error of any order. In 2D autofocus, the PGA process includes windowing, shifting and phase gradient estimation. Subsequently, some improved algorithms have also been proposed. In [27], quality PGA (QPGA) was proposed, which improves the reliability and efficiency of PGA by selecting prominent

units. In [28], weighted phase curvature autofocus (WPCA) was introduced to process repeat-pass SAR data. In [29], PGA was applied to TomoSAR imaging, and least squares estimation was used in the calculation of the phase gradient. Feng et al. employed PGA to solve the phase error calibration problem in MB CSAR imaging in 2019 [30]. Lu et al. proposed the network construction PGA (NC-PGA) method in 2021 [31], which constructs a Delaunay triangulation network using selected prominent units to estimate the initial height of the scatterers in the prominent units, thereby eliminating the need to estimate the shifts in the $LOS_{\perp}$ direction. It also effectively addresses the issue of phase errors at the edge of the aperture by dividing the imaging area into blocks for PGA processing. In 2024, Huang et al. [32] combined PGA with cumulative intensity projection registration (CIPR) to solve the vertical shift problem and enhanced the robustness of the $LOS_{\perp}$ position estimation of the strongest scatterer by performing multi-look processing on 2D images.

Based on the existing research studies, an improved PGA method for MB CSAR 3D imaging is proposed in this paper. This method is based on the idea of phase gradient estimation and improves the computational efficiency and the quality of phase error calibration by adopting a weighted PGA (WPGA) method and a new convergence condition for iterative phase error calibration. Firstly, this algorithm basically follows the principle of PGA, but the weights are calculated and applied to maximum likelihood (ML) estimation for phase error gradients to suppress prominent units with bad quality. Secondly, prominent units are selected with a new criterion based on the energy of the pixel stacks to achieve better estimation performance and lower computational cost. The amplitude dispersion index (ADI) criterion is not used due to the introduction of weights. Thirdly, the rate of change for the contrast is used as the convergence condition for iterative phase error calibration, which can effectively avoid the problem of slow convergence in some sub-apertures and shifts in the $LOS_{\perp}$ direction while ensuring the quality of autofocus.

The rest of this paper is organized as follows: Section 2 introduces the 3D imaging model and phase error model of the MB CSAR system. Section 3 describes the principles and processing procedures of the proposed autofocus method. In Section 4, the autofocus and time efficiency performance of the proposed method is verified by using a real, measured dataset compared with two other methods. Section 5 provides a conclusion of this paper.

## 2. MB CSAR Model

### *2.1. Three-Dimensional Imaging Model*

The imaging geometry of the MB CSAR system is shown in Figure 1. An airborne radar flies around the scene of interest along circular tracks and repeats $P$ passes at different altitudes. The azimuth angle of the radar is $\theta$, and the elevation angle of the $p$-th pass is $\varphi_p$ ($p = 1, 2, \ldots, P$). Achieving a 3D image requires four steps, including aperture dividing, sub-aperture 2D imaging, sub-aperture 3D imaging and sub-aperture 3D image accumulation.

Firstly, the whole circular aperture is divided into $M$ non-overlapping sub-apertures, each of which has a width of $\Delta\theta = 2\pi/M$ in the azimuth and contains the echo data collected from $P$ passes.

Secondly, a sub-aperture image stack of $P$ single-look complex (SLC) 2D images is formed within each sub-aperture. Since ideal circular tracks are difficult to obtain in practice and the back-projection algorithm (BPA) is applicable for any irregular flying tracks [33], the BPA is adopted in this process. The 2D image value at $(x', y')$ of the 2D ground plane image grid of the $p$-th pass is denoted by $g_p(x', y')$.

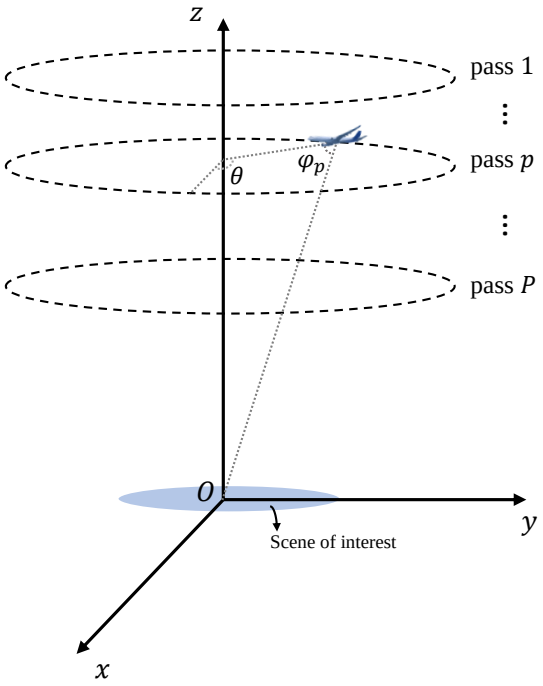



**Figure 1.** Imaging geometry of MB CSAR system.

Thirdly, the 3D image for each sub-aperture is generated based on the image stack. Under ideal conditions, $g_p(x', y')$ is added up by scatterers at different locations in the $LOS_\perp$ direction; thus, it can be expressed as follows:

$$g_p(x', y') = \sum_s \gamma(x', y', s) e^{j2\pi\sigma_p s}, \tag{1}$$

where $\sigma_p = 2\cos^2\overline{\varphi}\tan\varphi_p/\lambda$ denotes the spatial frequency for the $p$-th pass of the current sub-aperture, $\lambda$ is the wavelength and $\overline{\varphi}$ is the average elevation. $\gamma(x', y', s)$ denotes the scattering coefficient distribution in the $LOS_\perp$ direction. It should be noted that the $LOS_\perp$ direction changes over sub-apertures.

For each pixel stack at $(x', y')$, $N$ points are sampled along the $LOS_\perp$ direction from the range $[s_1, s_N]$. Let the steering vector be denoted by $\mathbf{a}(s_n) = [e^{j2\pi\sigma_1 s_n}, e^{j2\pi\sigma_2 s_n}, \ldots, e^{j2\pi\sigma_p s_n}]^T$. Steering vectors at different $LOS_\perp$ locations form $P \times N$ matrix $\mathbf{A}$, defined as $\mathbf{A} = [\mathbf{a}(s_1), \mathbf{a}(s_2), \ldots, \mathbf{a}(s_N)]$. Let $\boldsymbol{\gamma} = [\gamma(s_1), \gamma(s_2), \ldots, \gamma(s_N)]^T$ be the scattering coefficient distribution. With $P$ observations in one pixel stack, a vector $\mathbf{g} = [g_1, g_2, \ldots, g_P]^T$ can be built. Then, Equation (1) can be expressed in the following matrix form:

$$\mathbf{g} = \mathbf{A}\boldsymbol{\gamma} + \mathbf{n}, \tag{2}$$

where $\mathbf{n}$ denotes the $P \times 1$ noise vector. The 3D imaging problem is to obtain the scattering coefficient distribution $\boldsymbol{\gamma}$ from the observation $\mathbf{g}$. TomoSAR 3D imaging methods can be applied to acquire $\boldsymbol{\gamma}$, such as conventional beamforming (CBF), the iterative adaptive approach (IAA) and CS. Subsequently, a coordinate transformation from the local coordinate system $x' - y' - s$ to the global coordinate system $x - y - z$ is operated as follows:

$$\begin{cases} z = s\cos\overline{\varphi} \\ x = x' - z\tan\overline{\varphi}\cos\theta_m \\ y = y' - z\tan\overline{\varphi}\sin\theta_m, \end{cases} \tag{3}$$

where $\theta_m$ is the azimuth angle at the center of the $m$-th sub-aperture.

Finally, the full aperture 3D image $I(x,y,z)$ is acquired by accumulating all sub-aperture 3D images $I_m(x,y,z), m = 1,2,\ldots,M$. Since targets in the urban area are usually anisotropic, incoherent superposition is performed here, which is given by

$$I(x,y,z) = \sum_{m=1}^{M} |I_m(x,y,z)|. \tag{4}$$

### *2.2. Phase Calibration Model*

The ideal imaging model is discussed in Section 2.1. However, since position error during the movement of the radar platform and phase error between different passes exist and the measurement accuracy of the global positioning system (GPS) or other positioning sensors is insufficient, the imaging results are blurred, and further calibration is required before applying 3D imaging methods.

For a 2D SLC image stack, the phase error for the $p$-th pass at $(x',y')$ can be represented as $\phi_p$; let $\mathbf{p} = [e^{j\phi_1}, e^{j\phi_2}, \ldots, e^{j\phi_P}]^T$. The relationship between the phase error and 2D SLC images is expressed as follows:

$$\mathbf{g} = \mathbf{p} \odot \mathbf{A}\boldsymbol{\gamma} + \mathbf{n}. \tag{5}$$

The goal of phase error calibration is to estimate the phase $\phi_p$ in $\mathbf{p}$. In the case of a small scene, the phase error can usually be considered space-invariant, that is, the phase error does not change with the pixel position within the scene of interest. Under this assumption, the phase error can be estimated by combining different pixel stacks.

## 3. Proposed Autofocus Method

Phase error calibration is performed before 3D imaging in each sub-aperture. PGA is based on the assumption that the phase error is space-invariant within the scene of interest. The fundamental idea of PGA is to select prominent units from 2D SLC images and use them to estimate the phase error gradient along the $LOS_\perp$ direction. The phase error is then calculated with phase error gradient estimation. In this section, a new WPGA method is introduced to estimate the phase error with a new prominent unit selection criterion and a new convergence condition.

### *3.1. Weighted Phase Gradient Estimation*

Let us suppose that $K$ prominent units are selected for estimation. The estimation model of the pixel stack $\mathbf{g}_k$ at the $k$-th prominent unit is discussed as follows: The pixel value at the $p$-th pass is composed of the strongest scatterer and clutter, where the clutter includes other weak scatterers and noise. Let the clutter at the $p$-th pass of the $k$-th prominent unit be denoted by $c_{p,k}$. The pixel value obtained from the $p$-th pass can be expressed as follows:

$$g_{p,k} = \gamma_k e^{j(2\pi\sigma_p s_k + \phi_p)} + c_{p,k}, \tag{6}$$

where $\gamma_k$ is the scattering coefficient of the strongest scatterer and $s_k$ is the location of the strongest scatterer in the $LOS_\perp$ direction in the $k$-th prominent unit. The linear phase term $2\pi\sigma_p s_k$ is dominated by the strongest scatterer and can be removed by estimating the position of the strongest scatterer along the $LOS_\perp$ direction. The removal of this term is given by

$$\begin{aligned} g'_{p,k} &= g_{p,k} e^{-j2\pi\sigma_p s_k} \\ &= \gamma_k e^{j\phi_p} + c'_{p,k}, \end{aligned} \tag{7}$$

where $c'_{p,k} = c_{p,k} e^{-j2\pi\sigma_p s_k}$. After this processing is completed, only the phase error contributes to the phase term. Let $\mathbf{b}_p$ be the vector that contains all pixel value samples collected from $K$ prominent units at the $p$-th pass, which is shown as follows:

$$\mathbf{b}_p = [g'_{p,1}, g'_{p,2}, \ldots, g'_{p,K}]^T. \tag{8}$$

PGA estimates the phase error gradient between each two adjacent passes by using all chosen prominent units, thereby obtaining the phase error vector. Let the phase error gradient be denoted by $\widehat{\dot{\phi}}_p$, which is given by [25,30]

$$\begin{aligned}\widehat{\dot{\phi}}_p &= \arg\left(\mathbf{b}_p^H \mathbf{b}_{p+1}\right) \\ &= \arg\left[\sum_{k=1}^{K} (g'_{p,k})^* g'_{p+1,k}\right],\end{aligned} \tag{9}$$

where $\arg(\cdot)$ is the phase extraction operator, $(\cdot)^*$ is the conjugate operator and $p = 1, 2, \ldots, P-1$. All prominent units share the same weight in this estimation. However, the clutter in different prominent units varies. Consequently, the quality of the selected prominent units also varies. It is hoped that high-quality prominent units will give a greater contribution to the estimation result, whereas those of low quality will be suppressed. Therefore, WPGA is introduced to enhance the reliability of the estimation by giving different weights to different prominent units. Equation (9) is modified into weighted maximum likelihood (WML) estimation [34], which is shown as follows:

$$\widehat{\dot{\phi}}_p = \arg\left[\sum_{k=1}^{K} w_k (g'_{p,k})^* g'_{p+1,k}\right], \tag{10}$$

where $w_k$ is the weight given to the $k$-th prominent unit. The key of WPGA is to obtain a proper weight for each prominent unit. The weight is assigned with the signal-to-clutter ratio (SCR) in each prominent unit. Prominent units with a lower SCR are assigned lower weights, whereas those with a higher SCR are assigned higher weights. Before calculating the weights, several definitions need to be made. The SCR within the $k$-th prominent unit is denoted by $w_k$. Let us suppose that the amplitude of $g_{p,k}$ is $A_k(p)$, where $p = 1, 2, \ldots, P$. Let $b_k$ and $d_k$ be defined as follows:

$$b_k = E[A_k(p)] = \frac{1}{P} \sum_{p=1}^{P} A_k(p), \tag{11}$$

$$d_k = E[A_k^2(p)] = \frac{1}{P} \sum_{p=1}^{P} A_k^2(p). \tag{12}$$

Then, the weights can be estimated according to Equation (13), the detailed derivation of which can be found in [35].

$$w_k \approx \frac{d_k}{4(2b_k^2 - d_k) - 4b_k\sqrt{4b_k^2 - 3d_k}}. \tag{13}$$

This definition of weights can suppress those units with higher clutter power.

With the obtained phase error gradients, the phase error can be acquired by accumulating phase gradients, which is given by [30]

$$\widehat{\phi}_p = \begin{cases} 0, & p = 1 \\ \sum_{t=2}^{p} \widehat{\dot{\phi}}_t, & p = 2, 3, \ldots P. \end{cases} \tag{14}$$

### *3.2. Autofocus Algorithm Realization*

In the process of algorithm implementation, several important steps also need to be discussed, which are setting rules for choosing prominent units, eliminating the linear phase term caused by the strongest scatterer and iteratively performing autofocus. In the following analysis, a new criterion for prominent unit selection and a new convergence condition are proposed, and linear phase term elimination is also clarified.

#### 3.2.1. Prominent Unit Selection

Prominent unit selection in PGA usually adopts the ADI criterion, the purpose of which is to select the points with better stability [32]. In WPGA, this selection process can be omitted because the points with strong clutter power are suppressed during estimation. However, it causes too large a computational burden if all pixels are utilized. With the aim of better estimating performance and faster computation, a new selection criterion is designed for the process of WPGA.

Considering the signal model in Equation (6), each chosen prominent unit is expected to include a strong scatterer instead of only clutter. Strong scatterers are generally located in pixel stacks that have strong energy; hence, strong pixels can be simply reserved for phase error gradient estimation. The energy of each pixel stack is calculated as the sum of the square to the amplitude of $p$ pixels. An energy threshold $E_{th}$ is established to filter the pixels, and the reserved units meet the following condition:

$$E_k = \sum_{p=1}^{P} |g_{p,k}|^2 > E_{th}. \tag{15}$$

Additionally, prominent units can also be selected by reserving a certain number of the largest points in terms of energy $E_k$. It is noted that the threshold $E_{th}$ changes in different sub-apertures since the energy distribution in each sub-aperture varies.

#### 3.2.2. Linear Phase Term Elimination

The key to removing the linear phase term $2\pi\sigma_p s_k$ in Equation (7) is to obtain the location of the strongest scatterer in the $LOS_\perp$ direction. The method in TomoSAR is utilized to obtain the image along the $LOS_\perp$ direction, and the highest peak in the image $\gamma_k$ is taken as the estimated location of the strongest scatterer. CBF is adopted here, which can be expressed as follows:

$$\gamma_k(s_n) = \frac{\mathbf{a}_k^H(s_n)\mathbf{g}_k}{\mathbf{a}_k^H(s_n)\mathbf{a}_k(s_n)}, \tag{16}$$

where $\gamma_k(s_n)$ is the scattering coefficient estimated at $s_n$ in the $LOS_\perp$ direction in the $k$-th prominent unit and $\mathbf{a}_k(s_n)$ is the steering vector at $s_n$ in the $LOS_\perp$ direction in the $k$-th prominent unit. This estimation method only requires a single snapshot and has high speed.

#### 3.2.3. Convergence Condition

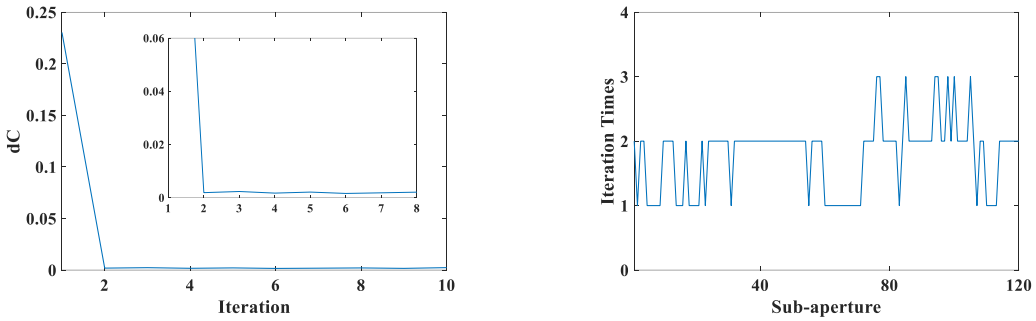
Generally, the PGA method reaches the convergence of iterations based on the root mean square (RMS) of the phase error difference between two adjacent iterations [30]. However, in some sub-apertures, it takes a few iterations to reach convergence, and the image quality is not improved in the latter iterations, only shifting along the $LOS_\perp$ direction. Inspired by optimization autofocus algorithms based on a certain criterion, a practical convergence condition is presented here, which is based on the contrast of $\gamma$ generated by the selected pixel stack. The definition of the contrast is given as [36]

$$C = \frac{\sqrt{\frac{1}{N}\sum_{n=1}^{N}(f_n - \frac{1}{N}\sum_{n=1}^{N} f_n)^2}}{\frac{1}{N}\sum_{n=1}^{N} f_n}, \tag{17}$$

where $f_n = |\gamma(s_n)|^2$ is the intensity. When the contrast of a selected prominent unit no longer increases, the iteration stops. The rate of change for the contrast $dC_i$ is defined as the proportion of the standard deviation and the mean of $\gamma$ along the $LOS_\perp$ direction. Then, a threshold $c_{th}$ is applied. When $dC_i$ is lower than this threshold, it is considered that the iteration can be terminated. The stopping condition is given by

$$dC_i = \frac{C_i - C_{i-1}}{C_i} < c_{th}. \tag{18}$$

Using this stopping condition can improve the image quality while effectively reducing the number of iterations, thereby reducing the overall processing computational burden. In addition, it can also suppress the shift along the $LOS_{\perp}$ direction. Convergence under this condition can be seen in Figure 2, which was obtained from the Gotcha dataset mentioned in Section 4.1. It can be seen that the iteration reaches fast convergence in Figure 2a and that the iteration times are not more than three in Figure 2b.




(**a**) (**b**)

**Figure 2.** The contrast-based convergence condition. (**a**) Convergence in a sub-aperture. (**b**) Iteration times of all sub-apertures.

Based on the above discussion, the flowchart of the proposed autofocus method is shown in Figure 3. The overall process can be summarized as the following steps: using the energy criterion to select prominent units, iteratively calculating the WML estimation of the phase gradient, obtaining the phase error estimation and using it for phase error calibration. Iteration stops when the changing rate of the contrast reaches the convergence condition.

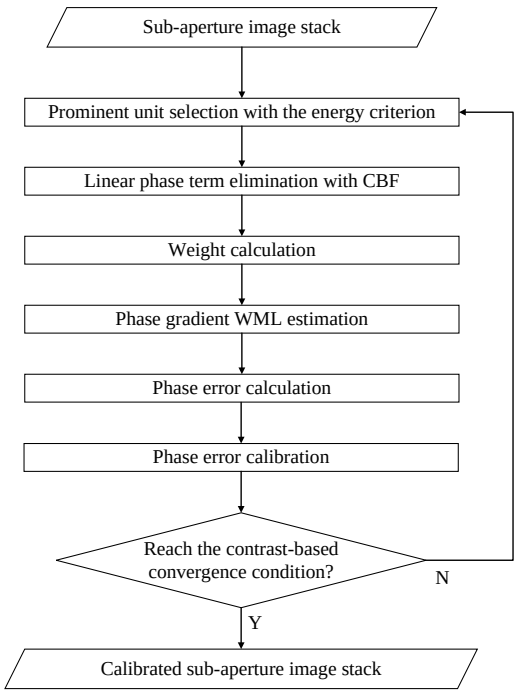



**Figure 3.** The flowchart of the proposed autofocus method.

## 4. Experimental Results and Discussion

In this section, the performance and feasibility of the proposed autofocus method are proved with real, measured MB CSAR data (Gotcha dataset) provided by the Air Force Research Lab (AFRL) [37], compared with the weighted least square (WLS) method and the PGA method. The experiments consisted of imaging results at four selected points in four different sub-apertures, contrast and entropy analysis for these four points, projections of 3D images and 3D images. The above-mentioned experiments were conducted in two areas of the scene. The time efficiency of the proposed autofocus method is also compared and analyzed.

### *4.1. Dataset Overview*

The proposed autofocus algorithm was applied to process the real, measured MB CSAR data "Gotcha Volumetric SAR Data Set, Version 1.0", which are the radar observation data of a real scene consisting of numerous civilian vehicles and calibration targets. The data were collected in the X-band with a bandwidth of 640 MHz and covered HH, HV, VH and VV polarizations. The flying tracks covered full 360° azimuth at eight different elevation angles, which are shown in Figure 4.

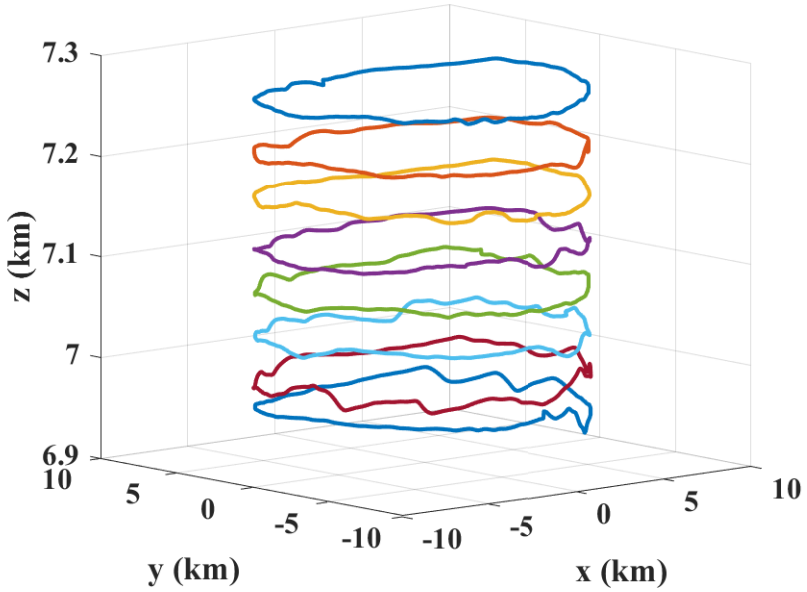



**Figure 4.** Radar tracks in the Gotcha dataset.

It can be found that the tracks are not regular circles.

The data collected from each flying pass contain 42,208∼43,068 samples in the cross range direction and 424∼434 samples in the range direction for each polarization. In our experiments, all of the samples in the HH polarization were used to form eight SLC images and to validate the performance of the proposed method.

The BPA was applied to process the data from the first pass in the HH polarization and form a 2D image to obtain a whole picture of the scene, as shown in Figure 5. It can be seen that it was an urban area of a parking lot with various vehicles.

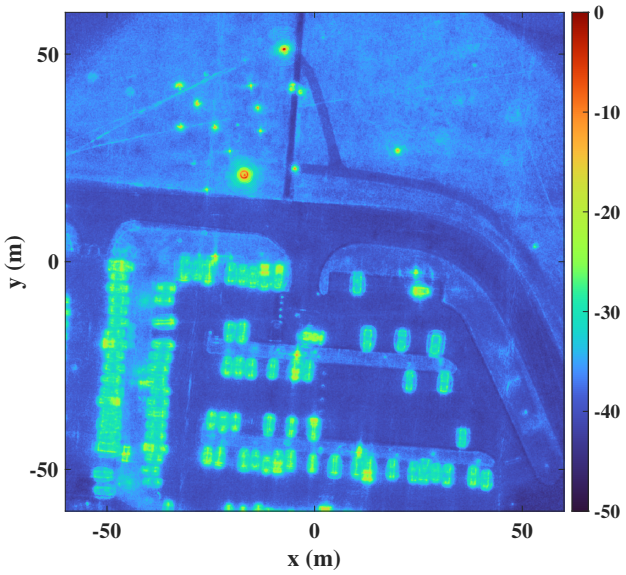



**Figure 5.** Two-dimensional image of the whole scene in HH polarization, obtained at the first pass.

### *4.2. Autofocus Results*

The CSAR data from all of eight passes in the HH polarization were processed. Firstly, the full 360° aperture was divided into 120 sub-apertures evenly, each of which had a sub-aperture of 3°, and the range of the elevation was $[43.7°, 45°]$. Then, in the processing of each sub-aperture, the BPA was utilized to form eight sub-aperture 2D SLC images, the resolution of which was 0.1 m in both directions. Autofocus was performed after 2D imaging and was followed by 3D imaging with CBF. Finally, the sub-aperture 3D images were incoherently accumulated to acquire the final 3D CSAR image. Two areas of the scene were selected for concrete analysis. The first area contained a Ford Taurus, and the second area contained a Toyota Camry. The optical images of these two cars are shown in Figure 6.




(**a**) (**b**)

**Figure 6.** Optical images of cars in chosen areas. (**a**) Ford Taurus; (**b**) Toyota Camry.

The first imaging area, which contained the Ford Taurus, was 8 m × 9.2 m in size. Experiments were conducted firstly on this area.

First, the calibration results of different calibration methods along the $LOS_{\perp}$ direction within the pixel stacks are demonstrated. Points $A, B, C$ and $D$ are four pixel stacks selected from 120 sub-apertures, as shown in Figure 7. Point A at (13.5 m, −16.5 m) was selected from the sub-aperture of 6°∼9°, point B at (14.1 m, −19.9 m) was selected from the sub-aperture of 348°∼351°, point C at (11.6 m, −15.7 m) was selected from the sub-aperture of 129°∼132°, and point D at (11 m, −20.4 m) was selected from the sub-aperture of 192°∼195°. The results of the three methods applied to the four points are shown in Figure 8a, 8b, 8c and 8d, respectively.

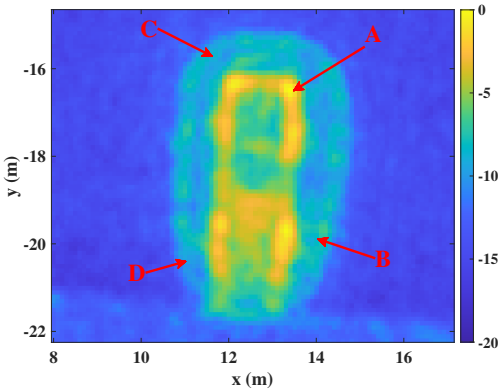



**Figure 7.** Locations of points A, B, C and D in the 2D SAR image of the Ford Taurus.

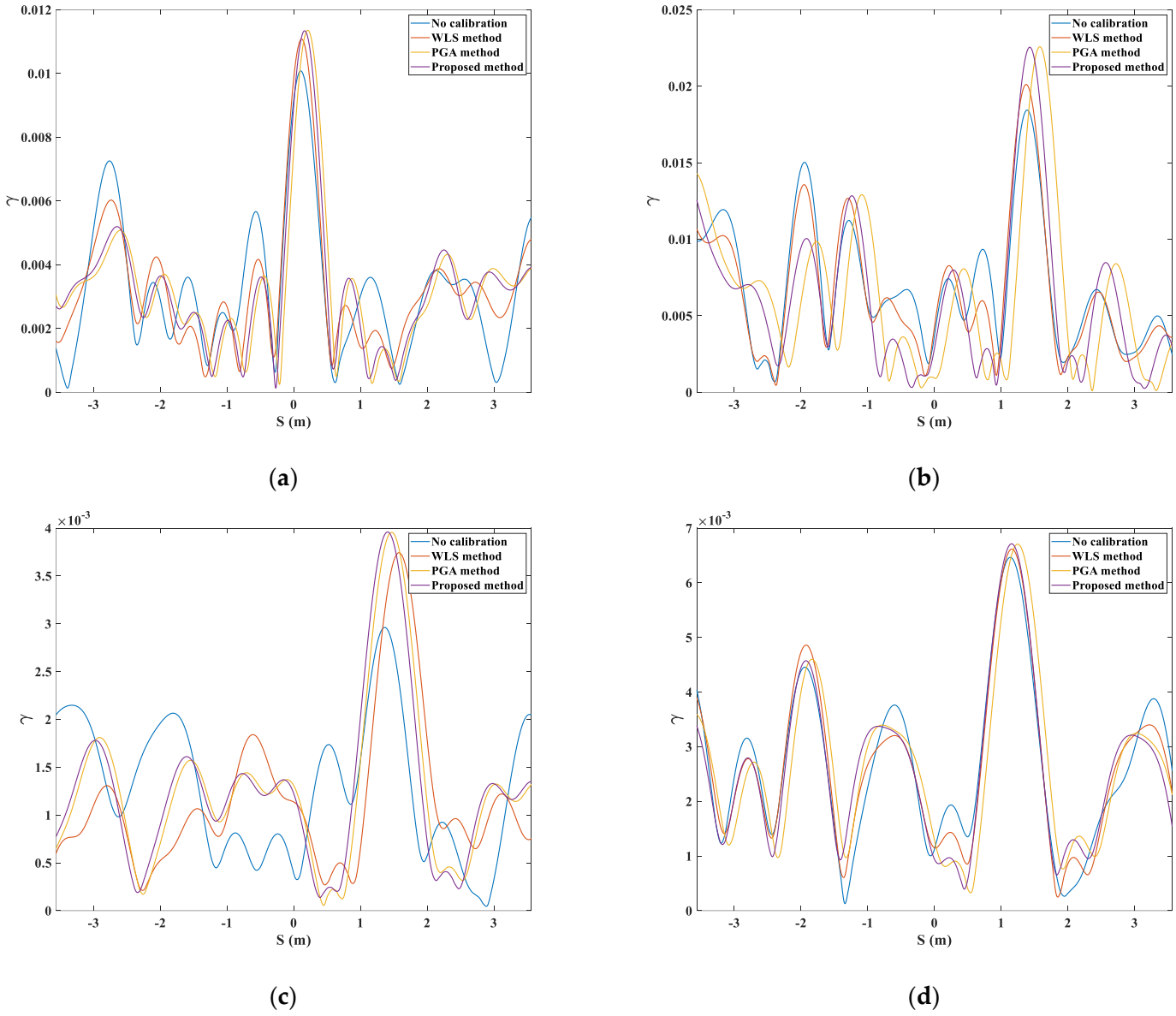



**Figure 8.** Imaging results of four selected points of the Ford Taurus area using different calibration methods. (**a**) Point A. (**b**) Point B. (**c**) Point C. (**d**) Point D.

For point A, the strongest scattering point was at the bottom of the car. According to Figure 8a, all three methods achieved good calibration results. The main lobe was increased, with the increases in the main lobe by the PGA method and the proposed method being similar and better than that by the WLS method. Most of the side lobes were also suppressed, with the suppression of the first side lobe by the PGA method and the proposed method being similar and better than that by the WLS method. A false target could be observed at −2.8 m on the left, caused by the ambiguity in the $LOS_{\perp}$ direction. The suppression of this false target by the PGA method was slightly better compared with the proposed method, while the WLS method showed poorer performance. The strongest scattering point for point B was on the roof of the car. For point B, the proposed method showed the best performance. Both the proposed method and the WLS method did not cause any shifts in the $LOS_{\perp}$ direction, while the result of the PGA method had a noticeable shift. In terms of the performance in main-lobe increase and side-lobe suppression, the proposed method and the PGA method were better than the WLS method. The strongest scattering point for point C was also on the roof of the car. For this point, the proposed method and PGA method performed well, while the WLS method had a lower main lobe and a significant shift. The strongest scattering point for point D was located at the top of the front of the car. For this point, the three methods showed similar performance in terms of main-lobe increase and side-lobe suppression, but the WLS method had a slightly lower main lobe, and the PGA method caused a slight shift. From the analysis of these selected points, the preliminary conclusion that can be drawn is that the proposed method has better and more stable calibration performance in different sub-apertures, followed by the PGA method. The WLS method has the poorest performance among these methods.

Contrast and entropy were calculated to better evaluate the performance of the three methods. The contrasts before and after the calibration were calculated according to Equation (17), while the entropy $E$ was calculated as follows:

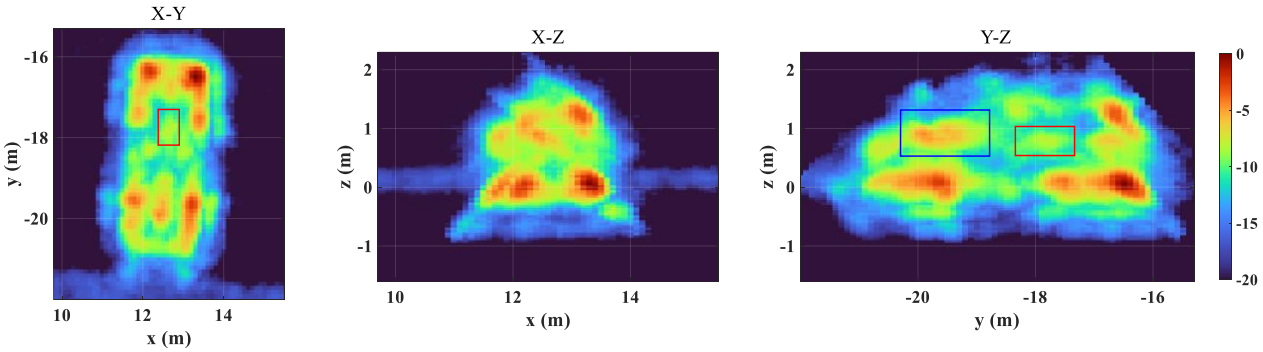
$$E = -\sum_{n=1}^{N} \frac{|f_n|^2}{\sum_{n=1}^{N}|f_n|^2} \ln \frac{|f_n|^2}{\sum_{n=1}^{N}|f_n|^2}. \tag{19}$$

The comparison of contrast and entropy is reported in Table 1. It can be seen that after calibration by the three methods, contrast was improved to varying degrees. The improvement of the WLS method was relatively smaller than that of the other two methods in points A, B and D. Although the WLS method showed the best contrast in point C, a noticeable shift could be observed. The contrast of the proposed method in points B and D was better than that of the PGA method, while in points A and C, it was slightly lower than that of the PGA method. The comparison of entropy shows similar results.

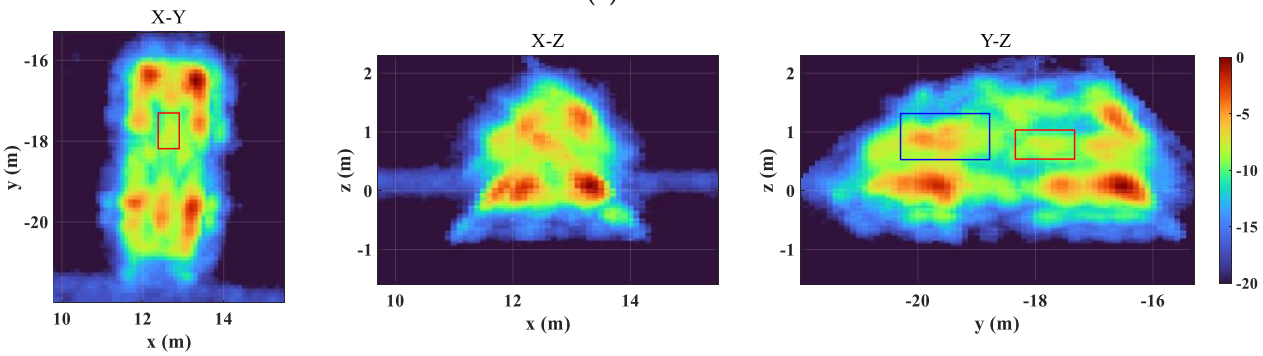
**Table 1.** Contrast and entropy comparison for the Ford Taurus after calibration with WLS, PGA and the proposed method.

| Methods | Point A | | Point B | | Point C | | Point D | |
|---|---|---|---|---|---|---|---|---|
| | Contrast | Entropy | Contrast | Entropy | Contrast | Entropy | Contrast | Entropy |
| No calibration | 2.7144 | 3.1704 | 2.1876 | 3.4985 | 1.6845 | 3.8251 | 2.0516 | 3.6227 |
| WLS method | 3.3208 | 2.8297 | 2.6516 | 3.2217 | 2.9569 | 2.9044 | 2.1448 | 3.5428 |
| PGA method | 3.5203 | 2.7080 | 3.0063 | 2.9720 | 2.8729 | 2.9871 | 2.2360 | 3.4989 |
| Proposed method | 3.4971 | 2.7239 | 3.1571 | 2.8787 | 2.8692 | 2.9936 | 2.2701 | 3.4722 |

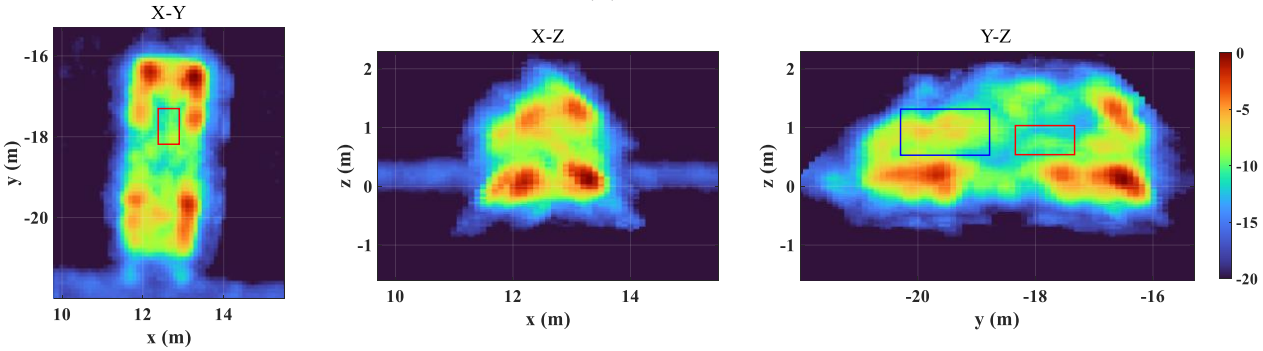
The comparison of the projection of 3D images can further confirm the above conclusion. Projections on the $x-y$, $x-z$ and $y-z$ planes of the 3D images with three autofocus methods are shown in Figure 9.



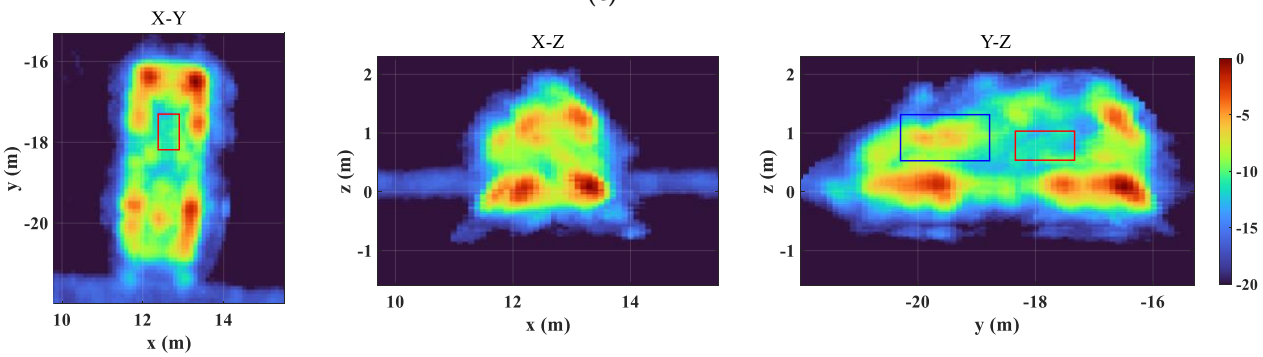

(**a**)




(**b**)




(**c**)




(**d**)

**Figure 9.** Projection of 3D images of the Ford Taurus. The left, middle and right columns are on the $x-y$, $x-z$ and $y-z$ planes, respectively. (**a**) No calibration. (**b**) WLS method. (**c**) PGA method. (**d**) Proposed method.

Firstly, projections on the $x-y$ plane are analyzed. Prior to calibration, there were noticeable false targets caused by the side lobes outside the car's contour during imaging. However, after utilizing three calibration methods, these false targets were suppressed to various degrees. Among these methods, the suppression capabilities of both the PGA method and the proposed method outperformed those of WLS method, likely due to comparatively weaker ability of the WLS method to enhance the main lobe and suppress the side lobes. Within the car's contour, false targets could be observed before calibration. Of the three methods, the proposed method demonstrated the most effective suppression, forming the cleanest image. The PGA method followed as the second most effective, while the WLS method was the least efficient, even amplifying the energy of some false targets. Similar phenomena could be observed in the $x-z$ plane and $y-z$ plane projections. Within the car's contour, the proposed method provided superior false-target suppression. Regarding the car's upper contour, highlighted by the blue box, both WLS and the proposed method enhanced the signal strength of this region, whereas the PGA method showed minimal enhancement. Additionally, the red box in the X-Y and Y-Z projections indicates a false target, where the proposed method also achieved superior suppression.

Next, 3D images with calibration were obtained by accumulating the sub-aperture 3D images from all the sub-apertures. Figure 10 shows 3D images without calibration, with WLS, PGA and the proposed method. From Figure 10a, it can be seen that before calibration, there were false targets in the areas in the red boxes, which was caused by high side lobes. The WLS method eliminated most false targets in this area, while PGA and the proposed method removed all the false targets. The area in the purple boxes is part of the bottom of the car, which was invisible before calibration. The WLS method failed to address this problem well, while PGA and the proposed method better reconstructed the bottom of the car. By observing the area in the green boxes, it can be seen that the proposed method produced a clearer image and performed better suppression of the false targets.

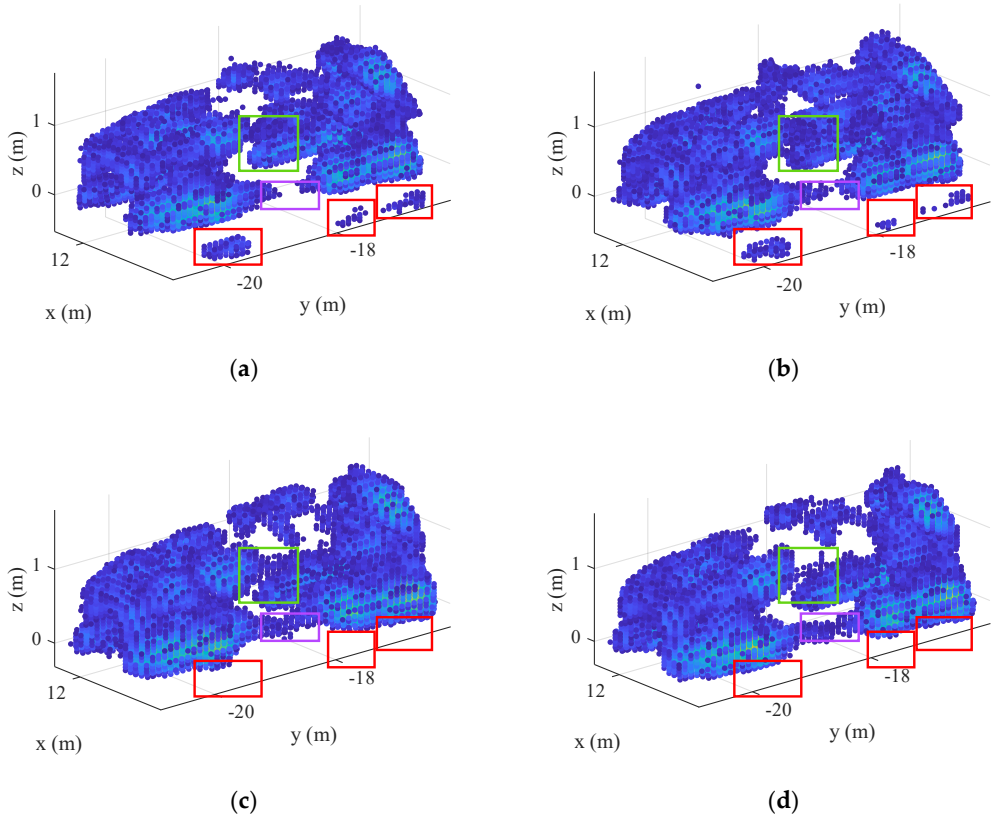



**Figure 10.** Three-dimensional images of Ford Taurus formed by different methods. (**a**) No calibration. (**b**) WLS method. (**c**) PGA method. (**d**) Proposed method.

Another area of 9.2 m × 7.6 m, which contained the Toyota Camry, in this scene was also used in experiments to prove the applicability of the proposed method. Four points, points E, F, G and H, were selected from 120 sub-apertures, where point E at (21.6 m, −16.7 m) was selected from the sub-aperture of 36°∼39°, point F at (19.2 m, −20.3 m) was selected from the sub-aperture of 183°∼186°, point G at (20.1 m, −20.7 m) was selected from the sub-aperture of 207°∼210° and point H at (21.6 m, −20.3 m) was selected from the sub-aperture of 342°∼345°. The locations of the four selected points are shown in Figure 11.

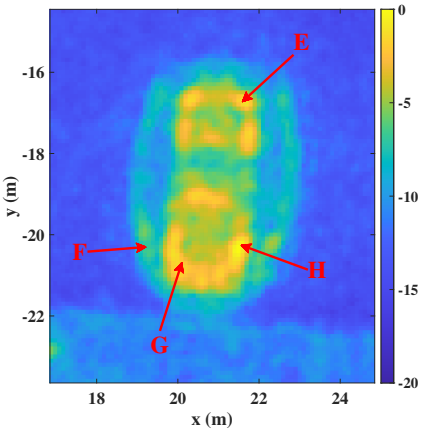
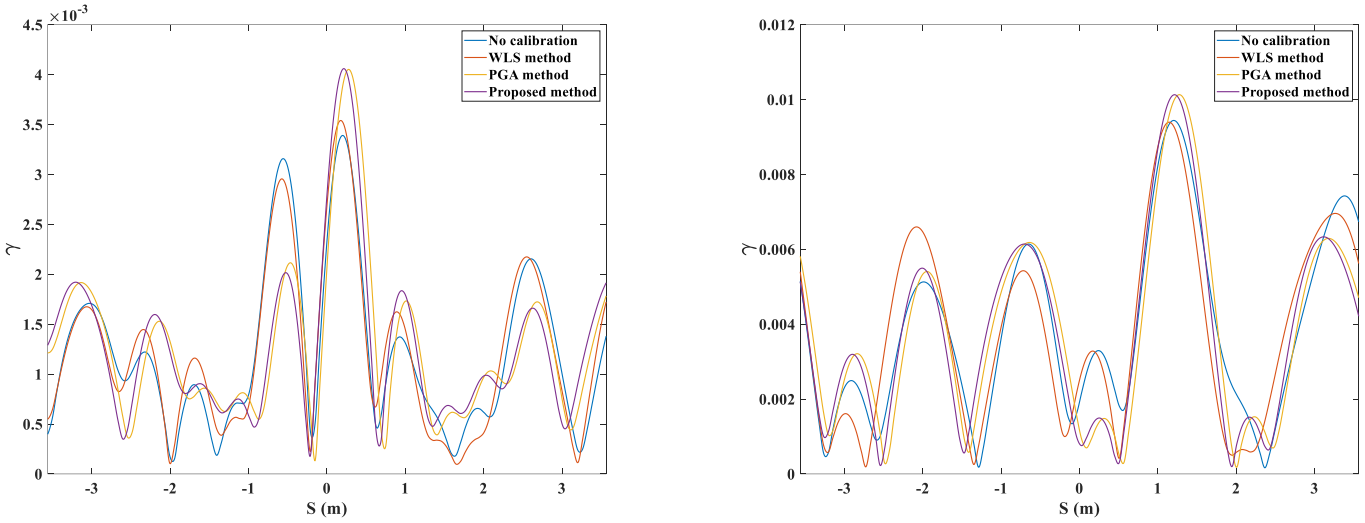



**Figure 11.** Locations of points E, F, G and H in the 2D SAR image of the Toyota Camry.

The calibration results of different calibration methods along the $LOS_{\perp}$ direction within the pixel stacks are shown in Figure 12. It can be seen from the results that the proposed method showed the best performance among the three calibration methods. The WLS method successfully calibrated the phase error in point H, had poor calibration in point E, caused a manifest shift in the $LOS_{\perp}$ direction in point G and failed to calibrate the phase error with a lower main lobe and a slight shift in point F. The PGA method effectively calibrated the phase error in points E, F and H. However, a manifest shift in the $LOS_{\perp}$ direction could be seen in point G. The proposed method successfully calibrated the phase error without shifts in all of the four points.




(**a**) (**b**)

**Figure 12.** *Cont.*

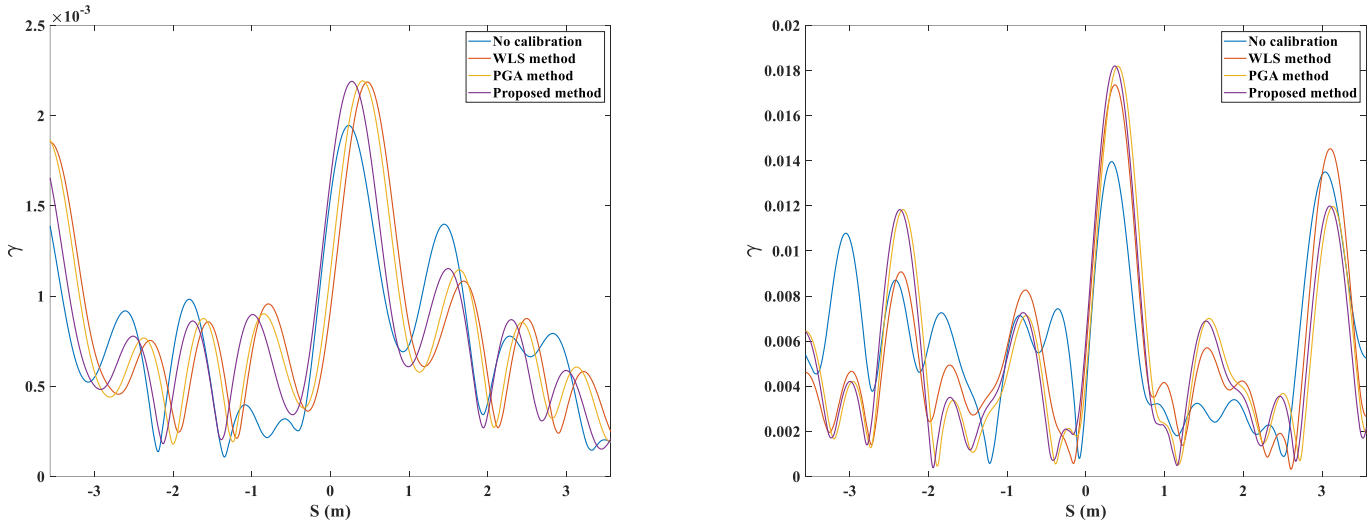



**Figure 12.** Imaging results of four selected points of the Toyota Camry area using different calibration methods. (**a**) Point E. (**b**) Point F. (**c**) Point G. (**d**) Point H.

In order to verify the performance quantitatively, contrast and entropy were also calculated and are reported in Table 2. The proposed method showed the best contrast increase and entropy decrease in points F, G and H, while in point E, the performance of the PGA method was slightly better than that of the proposed method. The WLS method demonstrated poorer performance than the PGA method and the proposed method.

**Table 2.** Contrast and entropy comparison for the Toyota Camry after calibration with WLS, PGA and the proposed method.

| Methods | Point E | | Point F | | Point G | | Point H | |
|---|---|---|---|---|---|---|---|---|
| | Contrast | Entropy | Contrast | Entropy | Contrast | Entropy | Contrast | Entropy |
| No calibration | 2.2758 | 3.3514 | 1.8996 | 3.6316 | 2.1949 | 3.4857 | 1.9020 | 3.6294 |
| WLS method | 2.3622 | 3.3563 | 1.7986 | 3.7130 | 2.3105 | 3.3290 | 2.5698 | 3.1309 |
| PGA method | 3.1402 | 2.9668 | 2.1437 | 3.5241 | 2.3701 | 3.2963 | 2.7867 | 3.0583 |
| Proposed method | 3.1327 | 2.9771 | 2.1514 | 3.5187 | 2.5369 | 3.2250 | 2.7904 | 3.0532 |

Three-dimensional images of the Toyota Camry with calibration were obtained by using all the sub-apertures. Figure 13 shows the 3D images without calibration, with WLS, PGA and the proposed method, and Figure 14 shows the projections of the 3D images. Similarly, the proposed method showed superior performance compared with the two other methods in the experiments on the second area.

Based on the above experiments and analyses on the two areas of the scene, it can be concluded that the proposed method has better calibration results among the three mentioned methods.

The time efficiency of the three autofocus methods was also compared. The computer's processor was an Intel Core i5-11400F, running at 2.60 GHz. WLS, PGA and the proposed method were executed on the Ford Taurus region in the same computing environment. It took an average computing time of 0.5188 s per sub-aperture to calibrate the phase error among 120 sub-apertures with the WLS method, 2.8701 s with PGA method, and only 0.0423 s with the proposed method. The time efficiency of the proposed method stems from the following factors: Firstly, the proposed method uses the energy criterion for selecting prominent units, i.e., Equation (15), whereas the PGA method uses the ADI criterion, according to [38], and in combination with the experimental scenario, the threshold of the ADI criterion here was

set to 0.2, which requires 3817∼5128 prominent units per sub-aperture on average in the image area of the Ford Taurus. In contrast, the energy criterion can achieve effective results when the number of prominent units is in the range of 300∼400. The reduction in the number of prominent units reduces the computational burden. In addition, the proposed method requires fewer iterations, not more than three in this area. Therefore, the proposed method has an advantage over the other two methods in terms of time efficiency.

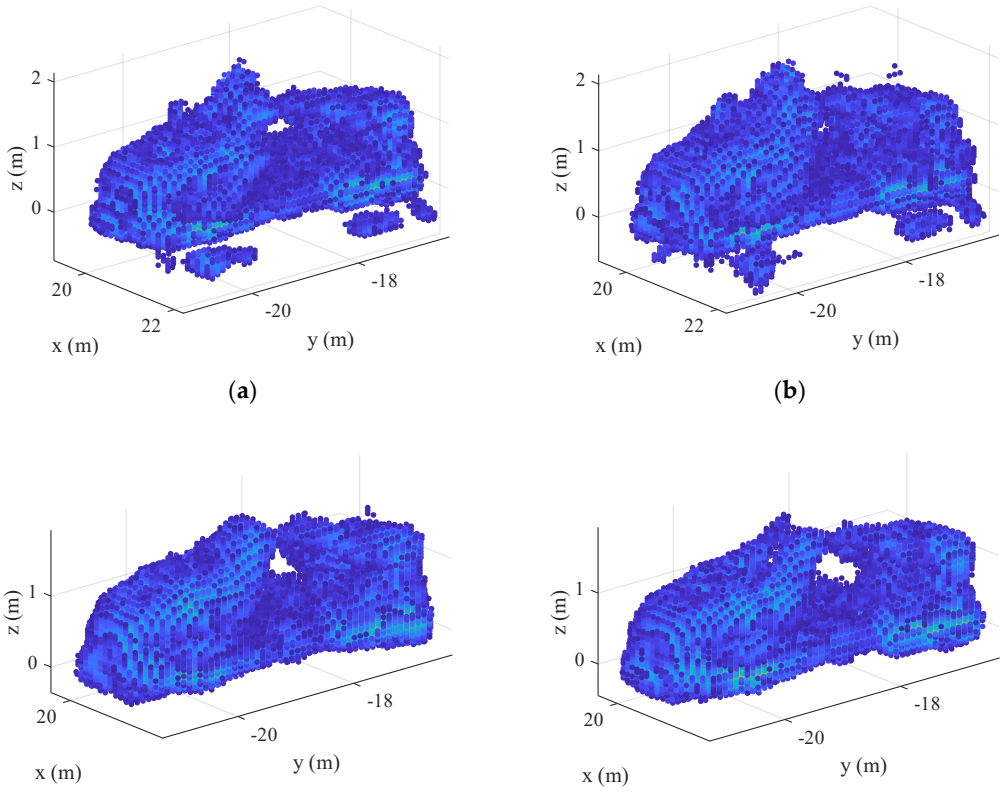
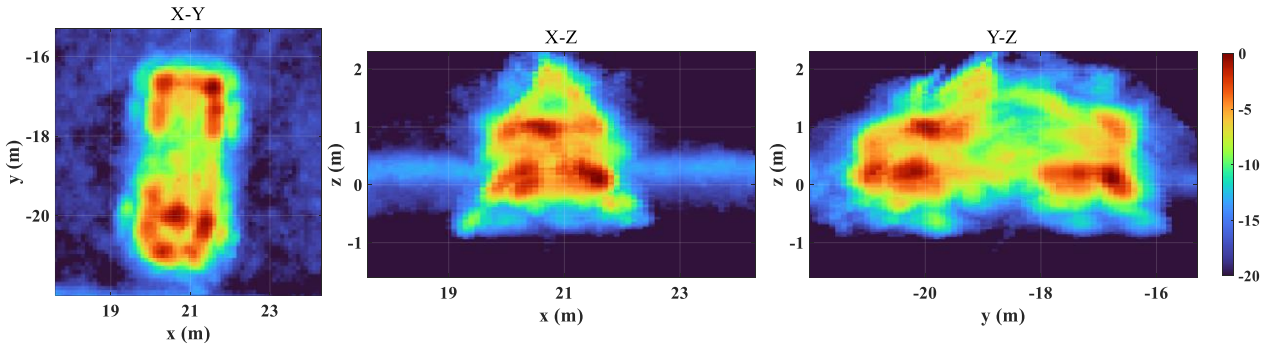



**Figure 13.** Three-dimensional images of the Toyota Camry formed by different methods. (**a**) No calibration. (**b**) WLS method. (**c**) PGA method. (**d**) Proposed method.




(**a**)

**Figure 14.** *Cont.*

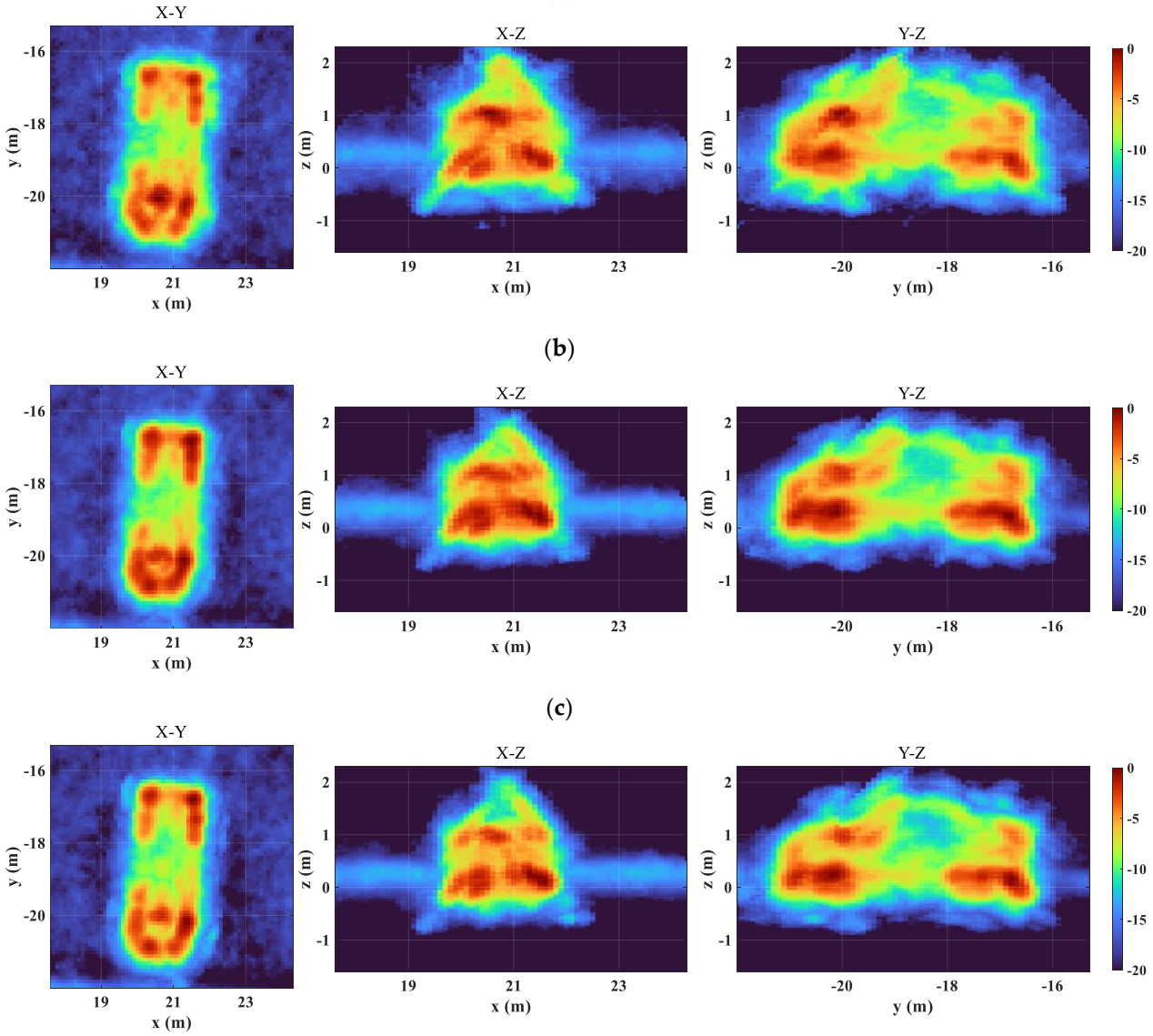



**Figure 14.** The projection of 3D images of the Toyota Camry. The left, middle and right columns are on the $x-y$, $x-z$ and $y-z$ planes, respectively. (**a**) No calibration. (**b**) WLS method. (**c**) PGA method. (**d**) Proposed method.

## 5. Conclusions

In this paper, an improved phase error calibration method for MB CSAR 3D imaging is proposed and discussed. Based on the ideas of the PGA method, the proposed method made some improvements, including a new method for the selection of prominent units, weighted phase gradient estimation and iteration controlled by a contrast criterion. Firstly, in prominent unit selection, prominent units with stronger energy are retained because they are more likely to contain strong scatterers. Additionally, in phase gradient estimation, a weight is calculated for each prominent unit to suppress those units that are strongly affected by clutter, where weight calculation is based on the estimation of the SCR in each unit. Finally, contrast is adopted as a practical condition for convergence to avoid shifts in the $LOS_{\perp}$ direction.

Several experiments were conducted to validate the performance of the proposed method based on real, measured CSAR data (Gotcha dataset) provided by the AFRL. A Ford Taurus car from a parking lot scene was selected to verify the effectiveness and

feasibility of the proposed method. It was proved that the proposed method can conduct valid phase calibration and has better performance compared with the WLS and PGA methods according to the calibration results of four pixel stacks from four sub-apertures, the projections of 3D images and 3D images of the Ford Taurus. Experimental results of a Toyota Camry car also proved that the proposed method has better performance. These phenomena indicate that the proposed method can be applied to acquire better phase error calibration results, hence acquiring better 3D SAR images. The proposed phase calibration method, as a part of MB CSAR 3D imaging technology, can be utilized in the 3D measurement and reconstruction of urban areas; thus, it can provide information support for road planning, urban construction, etc. In future work, we will focus on the application of the proposed method to other datasets and comparative experiments with other methods of the same category.

**Author Contributions:** Conceptualization, S.Y., H.X. and N.Z.; methodology, S.Y. and H.X.; software, S.Y. and H.X.; validation, S.Y. and H.X.; formal analysis, H.X., Z.L. and N.Z.; investigation, S.Y. and H.X.; resources, S.Y., H.X. and Y.Z.; data curation, S.Y., H.X. and Z.W.; writing—original draft preparation, S.Y. and H.X.; writing—review and editing, S.Y., H.X., Y.Z., Z.W., M.G. and P.Q.; visualization, S.Y. and H.X.; supervision, S.Y., H.X. and N.Z.; project administration, S.Y., H.X. and Z.L.; funding acquisition, H.X., Z.L. and N.Z. All authors have read and agreed to the published version of the manuscript.

**Funding:** This research was supported by Guangdong Basic and Applied Basic Research Foundation (grant No. 2023A1515011588); by Shenzhen Science and Technology Program (grant No. 202206193000001, 20220815171723002 and grant No. 202408133004377, 20240808223809002); by Fundamental Research Funds for the Central Universities, Sun Yat-sen University (grant No. 24qnpy202 and grant No. 24qnpy164); by China Postdoctoral Science Foundation (grant No. 2024M753740); by National Natural Science Foundation of China (grant No. 62203465 and grant No. 62201614); and Science and Technology Planning Project of Key Laboratory of Advanced IntelliSense Technology, Guangdong Science and Technology Department (grant No. 2023B1212060024). Hongtu Xie is the corresponding author.

**Data Availability Statement:** Data are contained within the article and can be made available by the authors.

**Acknowledgments:** The authors would like to thank the editors and reviewers for their very competent comments and helpful suggestions to improve this paper. Moreover, the authors would like to thank the American Air Force Research Lab (AFRL) for the Gotcha dataset.

**Conflicts of Interest:** The authors declare no conflicts of interest.

## References

1. Zhu, J.; Song, Y.; Jiang, N.; Xie, Z.; Fan, C.; Huang, X. Enhanced Doppler Resolution and Sidelobe Suppression Performance for Golay Complementary Waveforms. *Remote Sens.* **2023**, *15*, 2452. [CrossRef]
2. Xie, Z.; Wu, L.; Zhu, J.; Lops, M.; Huang, X.; Shankar, M.R.B. RIS-Aided Radar for Target Detection Clutter Region Analysis and Joint Active-Passive Design. *IEEE Trans. Signal Process.* **2024**, *72*, 1706–1723. [CrossRef]
3. Xie, Z.; Xu, Z.; Han, S.; Zhu, J.; Huang, X. Modulus Constrained Minimax Radar Code Design Against Target Interpulse Fluctuation. *IEEE Trans. Veh. Technol.* **2023**, *72*, 13671–13676. [CrossRef]
4. Liu, H.; Xie, H.; Gao, T.; Yi, S.; Zhang, Y. High-Precision Imaging and Dense Vehicle Target Detection Method for Airborne Single-Pass Circular Synthetic Aperture Radar. *IEEE J. Sel. Topics Appl. Earth Observ. Remote Sens.* **2024**, *17*, 15330–15343. [CrossRef]
5. Zhu, J.; Yin, T.; Guo, W.; Zhang, B.; Zhou, Z. An Underwater Target Azimuth Trajectory Enhancement Approach in BTR. *Appl. Acoust.* 2024, *accepted for publication*.
6. Wu, Z.; Xie, H.; Gao, T.; Zhang, Y.; Liu, H. Moving Target Shadow Detection Method Based on Improved ViBe in VideoSAR Images. *IEEE J. Sel. Topics Appl. Earth Observ. Remote Sens.* **2024**, *17*, 14575–14587. [CrossRef]
7. Zhu, J.; Xie, Z.; Jiang, N.; Song, Y.; Han, S.; Liu, W.; Huang, X. Delay-Doppler Map Shaping through Oversampled Complementary Sets for High Speed Target Detection. *Remote Sens.* **2024**, *16*, 2898. [CrossRef]
8. Moreira, A.; Prats-Iraola, P.; Younis, M.; Krieger, G.; Hajnsek, I.; Papathanassiou, K.P. A tutorial on synthetic aperture radar. *IEEE Geosci. Remote Sens. Mag.* **2013**, *1*, 6–43. [CrossRef]
9. Soumekh, M. Reconnaissance with slant plane circular SAR imaging. *IEEE Trans. Image Process.* **1996**, *5*, 1252–1265. [CrossRef]

10. Austin, C.D.; Ertin, E.; Moses, R.L. Sparse Signal Methods for 3-D Radar Imaging. *IEEE J. Sel. Topics Signal Process.* **2011**, *5*, 408–423. [CrossRef]
11. Han, D.; Zhou, L.; Jiao, Z.; Song, C.; Wu, Y. A Fast 3-D Imaging Method for Circular SAR Based on 3-D Back-Projection Algorithm. In Proceedings of the IEEE International Geoscience and Remote Sensing Symposium, Waikoloa, HI, USA, 26 September–2 October 2020; pp. 2368–2371.
12. Reigber, A.; Moreira, A. First demonstration of airborne SAR tomography using multibaseline L-band data. *IEEE Trans. Geosci. Remote Sens.* **2000**, *38*, 2142–2152. [CrossRef]
13. Ponce, O.; Prats-Iraola, P.; Scheiber, R.; Reigber, A.; Moreira, A. First Airborne Demonstration of Holographic SAR Tomography With Fully Polarimetric Multicircular Acquisitions at L-Band. *IEEE Trans. Geosci. Remote Sens.* **2016**, *54*, 6170–6196. [CrossRef]
14. Lombardini, F.; Reigber, A. Adaptive spectral estimation for multibaseline SAR tomography with airborne L-band data. In Proceedings of the IEEE International Geoscience and Remote Sensing Symposium, Toulouse, France, 21–25 July 2003; pp. 2014–2016.
15. Nannini, M.; Scheiber, R.; Moreira, A. Estimation of the Minimum Number of Tracks for SAR Tomography. *IEEE Trans. Geosci. Remote Sens.* **2009**, *47*, 531–543. [CrossRef]
16. Bao, Q.; Lin, Y.; Hong, W.; Shen, W.; Zhao, Y.; Peng, X. Holographic SAR Tomography Image Reconstruction by Combination of Adaptive Imaging and Sparse Bayesian Inference. *IEEE Geosci. Remote Sens. Lett.* **2017**, *14*, 1248–1252. [CrossRef]
17. Aghababaee, H.; Fornaro, G.; Schirinzi, G. Phase Calibration Based on Phase Derivative Constrained Optimization in Multibaseline SAR Tomography. *IEEE Trans. Geosci. Remote Sens.* **2018**, *56*, 6779–6791. [CrossRef]
18. Reigber, A.; Prats, P.; Mallorqui, J.J. Refined estimation of time-varying baseline errors in airborne SAR interferometry. *IEEE Geosci. Remote Sens. Lett.* **2006**, *3*, 145–149. [CrossRef]
19. Gatti, G.; Tebaldini, S.; Mariotti d'Alessandro, M.; Rocca, F. ALGAE: A Fast Algebraic Estimation of Interferogram Phase Offsets in Space-Varying Geometries. *IEEE Trans. Geosci. Remote Sens.* **2011**, *49*, 2343–2353. [CrossRef]
20. Tebaldini, S.; Rocca, F.; Mariotti d'Alessandro, M.; Ferro-Famil, L. Phase Calibration of Airborne Tomographic SAR Data via Phase Center Double Localization. *IEEE Trans. Geosci. Remote Sens.* **2016**, *54*, 1775–1792. [CrossRef]
21. Pardini, M.; Papathanassiou, K.; Bianco, V.; Iodice, A. Phase calibration of multibaseline SAR data based on a minimum entropy criterion. In Proceedings of the IEEE International Geoscience and Remote Sensing Symposium, Munich, Germany, 22–27 July 2012; pp. 5198–5201.
22. Fletcher, I.; Watts, C.; Miller, E.; Rabinkin, D. Minimum entropy autofocus for 3D SAR images from a UAV platform. In Proceedings of the IEEE Radar Conference, Philadelphia, PA, USA, 2–6 May 2016; pp. 1–5.
23. Ash, J.N. An Autofocus Method for Backprojection Imagery in Synthetic Aperture Radar. *IEEE Geosci. Remote Sens. Lett.* **2012**, *9*, 104–108. [CrossRef]
24. Feng, D. Research on Technologies of Multibaseline SAR ThreeDimensional Imaging. Ph.D. Thesis, National University of Defense Technology, Changsha, China, 2020.
25. Wahl, D.E.; Eichel, P.H.; Ghiglia, D.C.; Jakowatz, C.V. Phase Gradient Autofocus: A Robust Tool for High Resolution SAR Phase Correction. *IEEE Trans. Aerosp. Electron. Syst.* **1994**, *30*, 827–835. [CrossRef]
26. Wahl, D.E.; Jakowatz, C.V.; Thompson, P.A.; Ghiglia, D.C. New approach to strip-map SAR autofocus. In Proceedings of the IEEE 6th Digital Signal Processing Workshop, Yosemite National Park, CA, USA, 2–5 October 1994; pp. 53–56.
27. Chan, H.L.; Yeo, T.S. Noniterative quality phase-gradient autofocus (QPGA) algorithm for spotlight SAR imagery. *IEEE Trans. Geosci. Remote Sens.* **1998**, *36*, 1531–1539. [CrossRef]
28. Macedo, K.A.C.d.; Scheiber, R.; Moreira, A. An autofocus approach for residual motion errors with application to airborne repeat-pass SAR interferometry. In Proceedings of the IEEE International Geoscience and Remote Sensing Symposium, Barcelona, Spain, 23–28 July 2007; pp. 4886–4889.
29. Sun, X. Research on SAR Tomography and Differential SAR Tomography Imaging Technology. Ph.D. Thesis, National University of Defense Technology, Changsha, China, 2012.
30. Feng, D.; An, D.; Huang, X.; Li, Y. A Phase Calibration Method Based on Phase Gradient Autofocus for Airborne Holographic SAR Imaging. *IEEE Geosci. Remote Sens. Lett.* **2019**, *16*, 1864–1868. [CrossRef]
31. Lu, H.; Zhang, H.; Fan, H.; Liu, D.; Wang, J.; Wan, X.; Zhao, L.; Deng, Y.; Zhao, F.; Wang, R. Forest height retrieval using P-band airborne multi-baseline SAR data: A novel phase compensation method. *ISPRS J. Photogramm. Remote Sens.* **2021**, *175*, 99–118. [CrossRef]
32. Huang, F.; Feng, D.; Hua, Y.; Ge, S.; He, J.; Huang, X. Phase Calibration in Holographic Synthetic Aperture Radar: An Innovative Method for Vertical Shift Correction. *Remote Sens.* **2024**, *16*, 2728. [CrossRef]
33. Chen, L.; An, D.; Huang, X. A Backprojection-Based Imaging for Circular Synthetic Aperture Radar. *IEEE J. Sel. Top. Appl. Earth Obs. Remote Sens.* **2017**, *10*, 3547–3555. [CrossRef]
34. Zhang, L.; Qiao, Z.; Xing, M.; Yang, L.; Bao, Z. A Robust Motion Compensation Approach for UAV SAR Imagery. *IEEE Trans. Geosci. Remote Sens.* **2012**, *50*, 3202–3218. [CrossRef]
35. Ye, W.; Yeo, T.S.; Bao, Z. Weighted least-squares estimation of phase errors for SAR/ISAR autofocus. *IEEE Trans. Geosci. Remote Sens.* **1999**, *37*, 2487–2494. [CrossRef]
36. Cacciamano, A.; Giusti, E.; Capria, A.; Martorella, M.; Berizzi, F. Contrast-Optimization-Based Range-Profile Autofocus for Polarimetric Stepped-Frequency Radar. *IEEE Trans. Geosci. Remote Sens.* **2010**, *48*, 2049–2056. [CrossRef]

37. Casteel, C.H.; Gorham, L.A.; Minardi, M.J.; Scarborough, S.M.; Naidu, K.D.; Majumder, U.K. A Challenge Problem for 2D/3D Imaging of Targets from a Volumetric Data Set in an Urban Environment. In Proceedings of the SPIE, 14th Algorithms and Synthetic Aperture Radar Imaging, International Society for Optics and Photonics, Orlando, FL, USA, 9–13 April 2007; pp. 97–103.
38. Ma, P.; Lin, H. Robust Detection of Single and Double Persistent Scatterers in Urban Built Environments. *IEEE Trans. Geosci. Remote Sens.* **2016**, *54*, 2124–2139. [CrossRef]

**Disclaimer/Publisher's Note:** The statements, opinions and data contained in all publications are solely those of the individual author(s) and contributor(s) and not of MDPI and/or the editor(s). MDPI and/or the editor(s) disclaim responsibility for any injury to people or property resulting from any ideas, methods, instructions or products referred to in the content.